Advanced Materials & Sustainable Manufacturing

SCIEPublish

Article

Finite Volume Method and Statistical Analysis of Heat Transfer in Hybrid PCM Bricks Containing Paraffin, Zeolite, and Hydrogel Ice Pack

Wahyudin Wahyudin [1], Doddy Irawan [1,2,*], Muhammad Iwan [1], Gunarto Gunarto [1], Raudhatul Fadhilah [2], Indra Ramadhan [1] and Yeyen Dea Arisandi [1]

[1] Department of Mechanical Engineering, University of Muhammadiyah Pontianak, Pontianak 78124, West Kalimantan, Indonesia; 221210007@unmuhpnk.ac.id (W.W.); muhammad.iwan@unmuhpnk.ac.id (M.I.); gunarto@unmuhpnk.ac.id (G.G.); 221210046@unmuhpnk.ac.id (I.R.); 221210040@unmuhpnk.ac.id (Y.D.A.)

[2] Research Center of Energy Nanomaterials, University of Muhammadiyah Pontianak, Pontianak 78124, West Kalimantan, Indonesia; raudhatul.fadhilah@unmuhpnk.ac.id (R.F.)

* Corresponding author. E-mail: irawan.doddy@unmuhpnk.ac.id (D.I.)

Received: 11 August 2026; Revised: 23 September 2026; Accepted: 19 October 2026; Available online: 3 November 2026

ABSTRACT: This study evaluates the daytime thermal-regulation performance of a hybrid composite brick integrated with a phase change material (PCM) core containing paraffin, natural zeolite, and a hydrogel ice pack. A one-dimensional finite volume method (1D FVM) model with a 10-node through-thickness grid and an effective heat-capacity formulation was used to represent transient conduction and was validated against outdoor measurements collected at 15-min intervals from 06:00 to 18:00 over six consecutive days. The measured exterior surface reached 45.52 °C at 12:15, whereas the brick core reached 44.58 °C at 13:45, giving a 90-min peak-temperature time lag. The maximum exterior-to-core temperature difference was 7.88 °C and the maximum exterior-to-interior thermal decrement was 4.65 °C. The calculated conduction heat flux reached 32.50 W/m^2 during heat absorption and −4.76 W/m^2 during heat release. Model validation yielded MAE = 0.577 °C, RMSE = 0.788 °C, and R^2 = 0.994. Because the maximum core temperature only approached the lower end of the reported paraffin melting interval (44–60 °C), a linear phase-fraction interpretation indicates only the onset of melting (approximately 3.6% at the core peak), rather than complete PCM melting. The results therefore support the hybrid brick as a thermal-buffering wall concept while defining the scope of the reduced-order model: radiation and free convection are not solved as separate field equations but are embedded in the measured surface-temperature boundary conditions.

Keywords: Phase change material; Hybrid composite brick; Thermal insulation; Finite volume method; Transient heat transfer; Building envelope

1. Introduction

Heat transfer through the building envelope strongly influences indoor thermal comfort and cooling demand, particularly in tropical climates where wall and roof surfaces are exposed to intense daytime solar

© 2026 The authors. This is an open access article under the Creative Commons Attribution 4.0 International License (https://creativecommons.org/licenses/by/4.0/).

loading. Phase change materials (PCMs) are widely investigated for passive thermal regulation because they can store and release thermal energy over a relatively narrow temperature interval, thereby increasing the apparent heat-storage capacity of envelope components [1–3]. In buildings, PCMs have been incorporated into wallboards, plaster systems, concrete panels, hollow bricks, masonry cavities, roofs, and multilayer wall assemblies to attenuate indoor temperature fluctuations, delay heat penetration, and shift the peak thermal load to a later time [4–12].

A major limitation of organic PCMs such as paraffin is their low intrinsic thermal conductivity, commonly below 1 W/m·K and often approximately 0.1–0.4 W/m·K, which can slow charging and discharging [13,14]. Solid-liquid PCMs also require containment to reduce leakage and to maintain geometric stability during repeated melting and solidification. For this reason, PCM systems are commonly macro- or micro-encapsulated and integrated with porous matrices, fins, metal foams, or architected lattice structures that increase the heat-transfer area or provide higher-conductivity pathways. Recent numerical studies have shown that lattice structures can markedly enhance the effective conductivity of PCM domains, while encapsulated packed-bed configurations and finned PCM capsules can improve heat-transfer rates during charging and discharging [13,15]. These studies motivate the use of a stabilizing porous phase and a physically confined cavity in building applications, even when the objective is thermal buffering rather than rapid heat extraction.

In the present hybrid core, paraffin provides the principal phase-change storage mechanism, natural zeolite acts as a porous absorbent and shape-stabilizing matrix, and the hydrated hydrogel ice-pack component contributes high sensible heat capacity and transient thermal buffering. The hybrid material is macro-encapsulated inside brick cavities so that the wall element itself serves as the containment structure. This arrangement is intended to combine the high storage density of paraffin with the structural stabilization of zeolite and the high heat capacity of the hydrated gel, while avoiding direct exposure of molten paraffin to the external environment [3,4,9,16,17].

A numerical approach is required to quantify the through-thickness temperature distribution and heat flow within the composite brick. The finite volume method (FVM) is suitable because the discretized equations are derived from energy conservation over each control volume. The present model is intentionally one-dimensional because the specimen has a much larger length and width than thickness and the experimental sensors were arranged primarily along the thickness direction. Latent heat is represented using an effective or apparent heat-capacity approach so that the phase-change contribution can be included without explicitly tracking a moving solid-liquid interface [17–20].

The numerical domain is discretized into 10 nodes across the 6.5-cm thickness. Measured upper- and lower-surface temperatures are imposed as time-dependent Dirichlet boundary conditions, and the predicted internal temperature is compared with the measured brick-core temperature. This formulation is a reduced-order conduction model: radiative and convective exchanges are not solved as separate exterior flow or radiation fields; instead, their net influence on the specimen surfaces is contained in the experimentally measured boundary temperatures. Consequently, no momentum equation, enthalpy-porosity flow model, under-relaxation factor, or mushy-zone constant is required.

The novelty of this study lies in combining a three-component paraffin-zeolite-hydrogel core (40/30/30 wt%) with a macro-encapsulated brick panel and validating a simple 1D FVM model using repeated outdoor measurements under tropical daytime conditions. Compared with studies focused on single-PCM bricks, multilayer PCM walls, or high-conductivity packed-bed and lattice systems, the present work emphasizes a low-complexity hybrid building element and an experimentally driven reduced-order model. The main contributions are the quantification of thermal time lag, temperature damping, and conduction heat flux; statistical validation using MAE, RMSE, and R^2; and an explicit assessment of the extent of phase change and model limitations within the 12-h daytime test window.

2. Materials and Methods

2.1. Materials

The main materials used in this study were paraffin, zeolite, and a hydrogel ice pack component incorporated into composite bricks. Paraffin was selected as the phase change material because of its ability to absorb and release thermal energy during the phase transition process. Zeolite was used as a porous matrix that serves as a shape stabilizer, absorber, and heat-distribution medium within the composite structure. This material was also expected to reduce paraffin leakage during the liquid phase and improve the thermal stability of the composite. The hydrogel ice pack component was added to enhance sensible heat storage and delay the temperature rise in the brick core [3]. The integration of these three materials was designed to produce a composite brick capable of delaying heat propagation, increasing time lag, and reducing temperature fluctuations through its thermal storage capacity [6,7]. Physically, the hybrid PCM material was integrated into the concrete bricks to form a macro-encapsulated wall panel for passive thermal regulation [8,9].

The thermal properties used as the basis for the numerical analysis are summarized in Table 1. In response to the need for a more complete material description, the table now also reports representative viscosity, latent heat, thermal-expansion coefficient, and flash-point information when these properties are physically applicable. The added paraffin values are literature ranges for paraffin PCMs with phase-change temperatures near the range of interest and are not claimed as independent measurements of the specific batch used in this experiment [12,21–23]. The 1D conduction model uses an effective hybrid-core density of 1263 kg/m^3, a baseline effective specific heat of 2660 J/kg·K, and an effective thermal conductivity of 0.313 W/m·K. Viscosity, thermal expansion, and flash point are reported for material characterization but are not solver inputs because no fluid-flow or combustion model is solved. For the hybrid material, the nominal latent capacity associated with the 40 wt% paraffin fraction is approximately 64–84 kJ/kg of hybrid core when a paraffin latent heat of 160–210 kJ/kg is used; this value is an estimate rather than a DSC measurement of the composite.

Table 1. Thermal properties and main functions of materials in hybrid PCM wall systems.

Material	Density ρ [kg/m^3]	Specific Heat cp [J/kg·K]	k [W/m·K]	Phase-Change T [°C]	Viscosity μ [Pa·s]	Latent Heat LH [kJ/kg]	β [K^{-1}]; Flash Point [°C]	Function/Refs.
Paraffin wax	750–900	2100 (liq.); 2900 (sol.)	0.21–0.24	44–60	0.0038–0.0063 (liq.)	160–210	0.0006–0.00714; >190	Main PCM and latent storage [7,12,21–23]
Hydrogel ice pack	1020	3800–4180	0.56–0.60	~0 (water-rich); not activated in 25–45 °C test range	N/A (crosslinked gel)	N/A in tested range	N/A; aqueous/non-flammable	Sensible/transient storage [24,25]
Natural zeolite	~700 (bulk); 1990 (particle)	935–1050	0.14–0.15	N/A	N/A	N/A	N/A	Porous matrix and shape stabilizer [15,16]
Brick	1600–1920	840–1000	0.69–0.96	N/A	N/A	N/A	N/A	Building-envelope element [10,25,26]
Concrete	2200–2400	880	1.40–1.80	N/A	N/A	N/A	N/A	Reference construction material [26]

Hybrid PCM core (effective)	1263	2660 (baseline effective)	0.313	44–60 (paraffin contribution)	N/A	~64–84, estimated as 0.40 LH, paraffin	N/A; not measured for mixture	Equivalent composite; this study/estimate

Note: N/A = Not Applicable (the property is not relevant or not active within the tested temperature range).

2.2. Composite Wall Specimen Design

The specimen used in this study was a composite brick panel designed as a passive wall element as illustrated in Figure 1. The panel dimensions were 132 cm × 61 cm × 6.5 cm. The thickness of 6.5 cm was used as the main direction for one-dimensional heat transfer analysis. These dimensions were selected to provide relatively large length-to-thickness and width-to-thickness ratios, thereby minimizing edge effects and allowing heat propagation to be assumed to be dominant in the thickness direction.

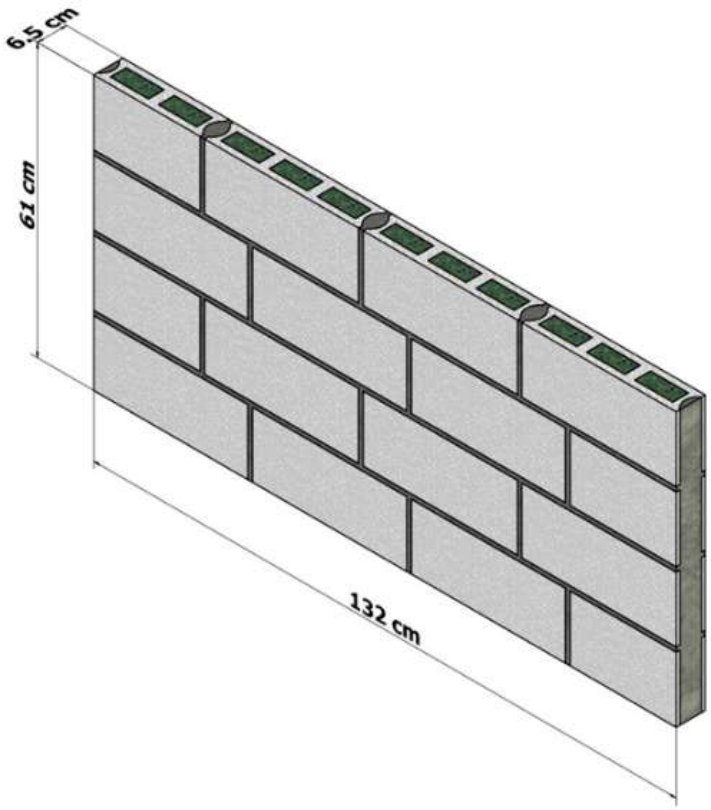


Figure 1. Wall Specimen Design. Schematic representation of the macro-encapsulated composite brick panel, illustrating the internal cavities where the hybrid PCM materials are integrated for the one-dimensional heat transfer analysis.

The primary heat transfer direction was assumed to occur from the upper surface to the brick core and then to the lower surface. Accordingly, the numerical model was simplified into a one-dimensional domain. This assumption was adopted because the most significant temperature gradient occurred through the specimen thickness, whereas temperature variations along the length and width directions were considered relatively small compared with the temperature difference between layers [27].

Temperature measurement points were placed at three main locations: the upper surface (T_{upper}), the brick core (T_{core}), and the lower surface (T_{lower}). In addition, ambient temperature ($T_{ambient}$) was measured as a supporting parameter to represent the surrounding thermal conditions during testing. The placement of sensors at different depths was intended to observe heat penetration, peak temperature delay, and thermal damping between layers [11].

2.3. Specimen Fabrication Method

The hybrid phase change material (PCM) core was prepared with a mass fraction distribution of 40% paraffin, 30% natural zeolite, and 30% hydrogel ice pack; the percentages refer to the total mass of the hybrid core. The preparation sequence was organized so that each constituent was brought to a suitable physical state before blending. First, the hydrogel component was hydrated by immersion in water for 3–5 min until volumetric swelling was achieved. In parallel, the paraffin wax was heated above its melting range until a homogeneous liquid phase was obtained. The natural zeolite was mechanically crushed to a non-sieved, multi-graded powder and stored in a desiccated condition before use so that uncontrolled moisture uptake was minimized.

For blending, the hydrated hydrogel and zeolite were first distributed throughout the mixing container, after which molten paraffin was added gradually while the mixture was continuously redistributed to promote contact between the liquid PCM and the porous mineral phase. The zeolite therefore acted as an absorbent and shape-stabilizing skeleton, while the hydrated gel occupied the remaining interparticle volume and contributed high sensible heat capacity. Mixing was continued until a stable semi-dry composite consistency was obtained. The hybrid material was then introduced into the brick cavities in successive portions and compacted to reduce entrapped air voids as illustrated in Figure 2. After the cavities were filled, the assembled panel was allowed to thermally stabilize in the conditioned environment before outdoor testing. The brick cavity provides macro-encapsulation of the hybrid material, while the zeolite reduces the mobility of liquid paraffin inside the cavity. This description reflects the preparation operations used in the study and avoids introducing unrecorded mixing speed or process temperature values that were not measured as independent experimental variables.

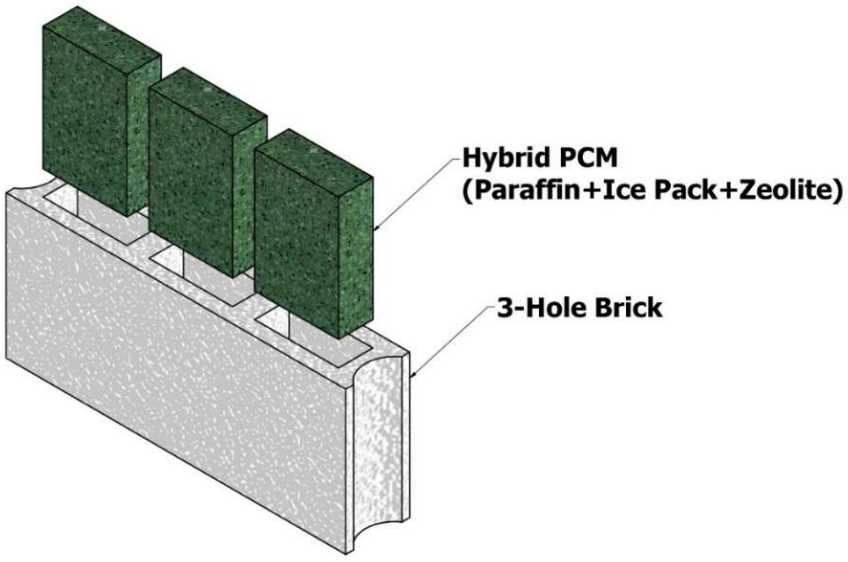


Figure 2. Fabrication Method. Illustration of the placement of hybrid PCM material inside a brick cavity.

2.4. Experimental Setup

The outdoor experimental campaign was conducted over six consecutive days. Thermal data were recorded at 15-min intervals between 06:00 and 18:00, yielding 49 data points per daytime cycle. Calibrated K-type thermocouples connected to a multi-channel data logger measured the upper surface temperature (T_{upper}), brick-core temperature (T_{core}), lower surface temperature (T_{lower}), and ambient temperature ($T_{ambient}$). The 06:00–18:00 interval was selected to capture the complete daytime solar-heating period and the beginning of the afternoon heat-release stage, which are the periods most directly related to cooling-load mitigation in the tested tropical environment as illustrated in Figure 3. The study therefore does not claim

to represent a complete 24-h charge-discharge cycle or full nocturnal resolidification. The measured temperature histories were subsequently used to validate the 1D FVM model and to calculate heat flux and statistical error indicators.

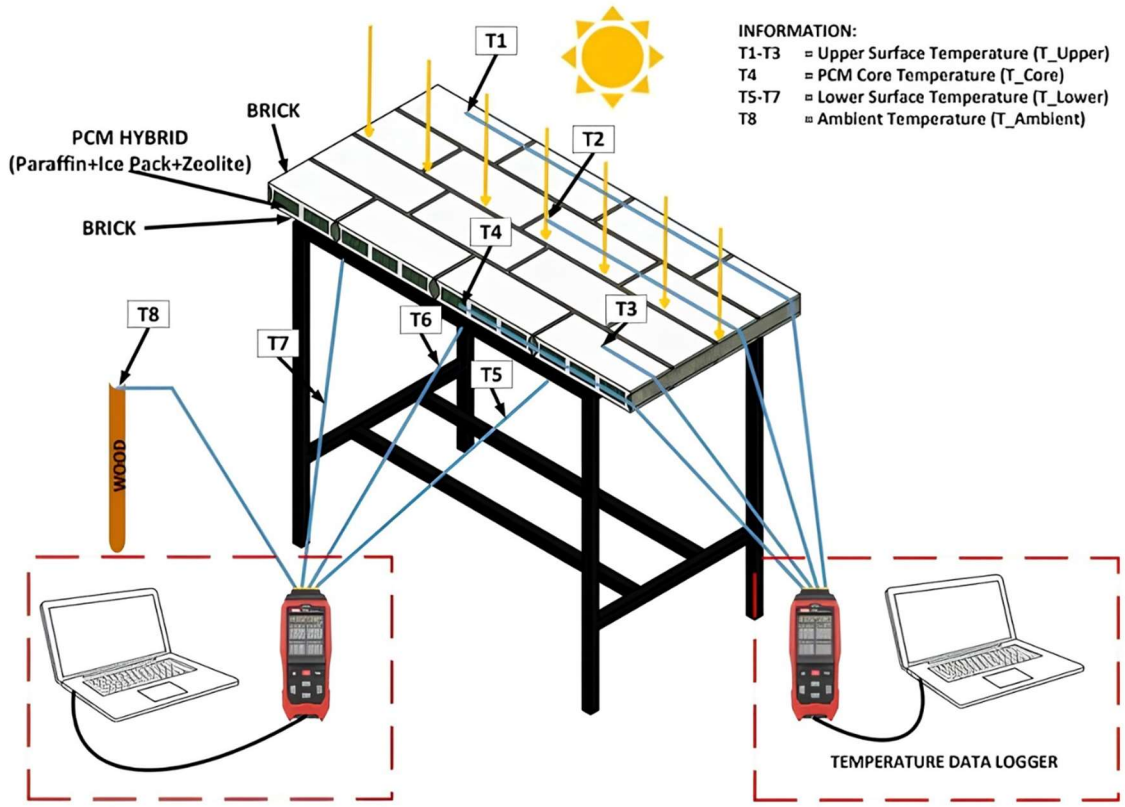


Figure 3. Experimental Setup. Photographic representation of the outdoor testing apparatus, illustrating the multi-channel data logger and thermocouple sensors affixed to the hybrid PCM composite brick for real-time transient temperature monitoring.

2.5. One-Dimensional Model Assumptions

The numerical model is a reduced-order transient-conduction model through the brick thickness. The physical assumptions and their implications are summarized in Table 2 to make the treatment of phase change, convection, radiation, and dimensionality explicit.

For interpretation of the PCM state, the revised manuscript uses a linear phase-fraction diagnostic consistent with the reported paraffin transition interval: $f_l = 0$ for $T \leq T_s$, $f_l = (T - T_s)/(T_l - T_s)$ for $T_s < T < T_l$, and $f_l = 1$ for $T \geq T_l$, with $T_s = 44$ °C and $T_l = 60$ °C. Within an apparent-heat-capacity representation, the latent contribution may be written as $L_{eff}/(T_l - T_s)$, where $L_{eff} = w_p L_p$ and $w_p = 0.40$ is the paraffin mass fraction. This phase-fraction expression is used to interpret the extent of melting; it does not introduce fluid velocity, buoyancy, or a mushy-zone constant into the 1D conduction solver.

Based on these assumptions, the governing equation for one-dimensional transient heat conduction can be expressed as follows:

$$\rho c_{p,eff} \frac{\partial T}{\partial t} = \frac{\partial}{\partial x}\left(k \frac{\partial T}{\partial x}\right) \quad (1)$$

For homogeneous materials with a constant k, the equation becomes:

$$\rho c_{p,eff} \frac{\partial T}{\partial t} = k \frac{\partial^2 T}{\partial x^2} \quad (2)$$

or:

$$\frac{\partial T}{\partial t} = \alpha \frac{\partial^2 T}{\partial x^2} \tag{3}$$

with:

$$\alpha = \frac{k}{\rho c_{p,eff}} \tag{4}$$

where ρ is material density (kg/m^3), $c_{p,eff}$ is the effective specific heat capacity (J/kg·K), k is thermal conductivity (W/m·K), $\alpha = k/(\rho c_{p,eff})$ is thermal diffusivity (m^2/s), T is temperature (°C or K), t is time (s), and x is the through-thickness coordinate (m).

Table 2. Solver setup and physical assumptions used in the 1D FVM model.

Item	Setting Used in This Study	Interpretation/Consequence
Dimensionality	1D through thickness, x	Length- and width-direction gradients are neglected; no 2D/3D contour field is implied.
Governing transport	Transient heat conduction	No momentum equation is solved inside the equivalent composite.
Material representation	Homogeneous effective core	ρ and k are treated as constant effective properties; $c_{p,eff}$ represents storage behavior.
Phase change	Effective/apparent heat-capacity treatment	Latent storage is represented without tracking a moving interface.
Radiation and free convection	Not solved as separate field equations	Their net influence on the specimen is embedded in the measured surface-temperature Dirichlet boundaries.
Mushy-zone constant	Not applicable	No enthalpy-porosity momentum sink or liquid-flow solution is used.
Spatial discretization	10 nodes across L = 0.065 m; $\Delta x \approx$ 0.00722 m	Uniform control-volume grid.
Spatial scheme	Central-difference face gradients	Second-order symmetric approximation for conduction gradients.
Time scheme	Explicit forward update; Δt = 150 s	Six internal solver steps per 900-s experimental sampling interval.
Under-relaxation factor	Not applicable	The explicit non-iterative update does not use pressure/velocity/energy under-relaxation.
Numerical acceptance	$Fo \leq 0.5$ and bounded temperatures	No residual-based iterative convergence criterion is required.
Internal heat generation	None	Source term $S_u = 0$ for the present model.

2.6. Domain Discretization with the Finite Volume Method 1D

The brick domain along the thickness direction, L, was divided into uniform control volumes with a spatial interval of Δx, as illustrated in Figure 4. Each control volume has a central node P, which is bounded by the west node W and the east node E. The energy conservation equation was integrated over each control volume from the west face to the east face and over the selected time interval. By applying the divergence theorem, the transient heat conduction equation was transformed into a discretized finite volume form.

The physical domain was partitioned into 10 computational nodes across the total thickness L = 0.065 m. With nine node-to-node intervals, the uniform spacing is $\Delta x = L/(N - 1) = 0.065/9 = 0.00722$ m (approximately 0.722 cm). The grid therefore resolves the predominant through-thickness temperature gradient while retaining the reduced-order character of the model. The present archived numerical results were generated on this 10-node grid; consequently, the revised manuscript does not claim a formal output-based mesh-independence study that was not performed in the original calculation set. Instead, the node count, spacing, and explicit stability restriction are now reported transparently. A rigorous future grid-

verification sequence should repeat the same boundary-value problem at successively refined N while reducing Δt to maintain $Fo \leq 0.5$.

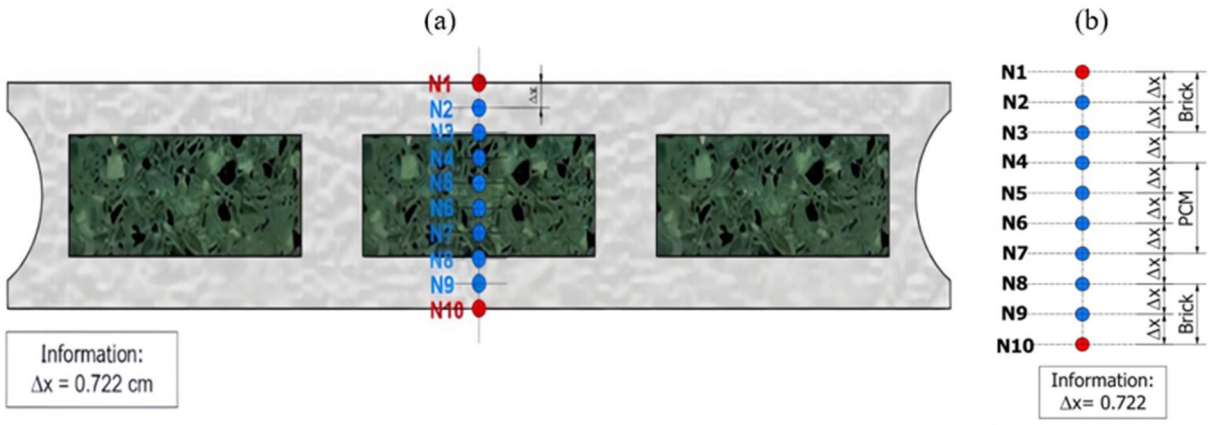


Figure 4. Spatial Discretization of the Composite Brick. (**a**) The macroscopic physical domain illustrating the predominant one-dimensional heat propagation path across the total thickness, L. (**b**) The corresponding 10-node computational grid formulated via the Finite Volume Method, highlighting the uniform spatial increment (Δx) and the localized control volume configuration (W, P, E) utilized for the numerical integration of the energy conservation equation.

This discretized modeling results in:

$$\int_t^{t+\Delta t}\int_w^e \rho\, c_{p,eff} A \frac{\partial T}{\partial t} dx dt = \int_t^{t+\Delta t}\int_w^e \frac{\partial}{\partial x}\left(kA\frac{\partial T}{\partial x}\right) dx dt \tag{5}$$

Once the divergence theorem is defined, the integral form becomes:

$$\rho c_{p,eff} A\Delta x(T_P^{n+1} - T_P^n) = \int_t^{t+\Delta t}\left[\left(kA\frac{\partial T}{\partial x}\right)_e - \left(kA\frac{\partial T}{\partial x}\right)_w\right] dt \tag{6}$$

where ρ is material density (kg/m^3), $c_{p,eff}$ is effective specific heat capacity (J/kg·K), A is the heat-transfer cross-sectional area (m^2), Δx is the control-volume length (m), Δt is the time step (s), T_P^{n+1} is the temperature at node P at the next time step, and T_P^n is the temperature at node P at the current time step.

2.7. Temperature Gradient Approximation and Discrete Equation

The temperature gradients at the east and west faces were approximated using the central difference scheme. Substituting these approximations into the integrated energy conservation equation yields the explicit finite volume formulation. After simplification, the temperature at node P for the next time step can be calculated from the temperatures of the neighboring nodes at the current time step [19].

$$\left(kA\frac{\partial T}{\partial x}\right)_e \approx kA\frac{T_E^n - T_P^n}{\Delta x} \tag{7}$$

$$\left(kA\frac{\partial T}{\partial x}\right)_w \approx kA\frac{T_P^n - T_W^{\Delta}x}{\Delta x} \tag{8}$$

The substitution of these two approximations into the energy conservation equation yields:

$$\rho c_{p,eff} A\Delta x(T_P^{n+1} - T_P^n) = \left[kA\frac{T_E^n - T_P^n}{\Delta x} - kA\frac{T_P^n - T_W^n}{\Delta x}\right] \tag{9}$$

or after simplification:

$$T_P^{n+1} = T_P^n + \frac{k\Delta t}{\rho c_{p,eff}(\Delta x)^2}(T_E^n - 2T_P^n + T_W^n) \tag{10}$$

If a Fourier number is defined as:

$$T_P^{n+1} = T_P^n + Fo(T_E^n - 2T_P^n + T_W^n) \tag{11}$$

For explicit schemes to be numerically stable, the following conditions must be met:

$$Fo \leq \frac{1}{2} \tag{12}$$

The explicit numerical scheme is governed by the Fourier number $Fo = \alpha\Delta t/\Delta x^2$, which must not exceed 0.5 for the present 1D explicit conduction update. Using k = 0.313 W/m·K, ρ = 1263 kg/m^3, c_p = 2660 J/kg·K, and Δx = 0.00722 m gives $\alpha = 9.32 \times 10^{-8}$ m^2/s. At the selected Δt = 150 s, Fo = 0.268, which satisfies the stability criterion and provides six numerical substeps within each 900-s measurement interval. Table 3 shows the stability screening used to select the time step. This screening demonstrates stability but is not presented as a substitute for a formal output-based time-step independence study; the revised manuscript therefore avoids claiming numerical independence that is not supported by archived refined-step solver outputs.

Table 3. Time-step stability screening for the 10-node explicit FVM grid.

Candidate Δt [s]	Fourier Number *Fo*	Assessment
900	1.608	Unstable for explicit scheme
450	0.804	Unstable
300	0.536	Slightly above stability limit
150	0.268	Stable; selected in this study
75	0.134	Stable; refinement candidate for future independence check
37.5	0.067	Stable; further refinement candidate

2.8. General Forms of the FVM Equation

In addition to the explicit update used in the calculations, the conservative coefficient form of the 1D finite volume equation is retained below to show the relationship between the central node and its east and west neighbors. No iterative linear-system solver was used for the reported explicit calculations; consequently, under-relaxation factors and residual convergence tolerances are not applicable to the implemented time-marching scheme [19].

$$a_P T_P^{n+1} = a_W T_W^n + a_E T_E^n + b \tag{13}$$

With coefficients defined as:

$$a_P = \frac{\rho c_{p,eff}\Delta x}{\Delta t} \tag{14}$$

$$a_W = a_E = \frac{k}{\Delta x} \tag{15}$$

$$b = S_u + (a_P^0)T_P^n \tag{16}$$

where a_P, a_W, and a_E are the discretization coefficients for the central, west, and east nodes; b is the contribution from the previous time level and any constant source term; and S_u denotes the linear external heat-source contribution, which is zero in the present model.

This formulation is used to show the general conservative form of the finite volume method, although the main implementation in this study focuses on an explicit scheme to facilitate comparison with experimental data.

2.9. Initial Conditions and Boundary Conditions

The initial temperature field was assumed uniform and was initialized from the first measured temperatures at the start of the daytime cycle (approximately 25 °C). The two specimen surfaces were prescribed based on measured temperatures, yielding time-dependent Dirichlet boundary conditions. The boundary treatment is summarized in Table 4.

$$T(x, 0) = T_0 \tag{17}$$

The use of measured surface temperatures as Dirichlet boundary values is deliberate: it allows the internal conduction model to be driven by the actual thermal response of the outdoor specimen without requiring separately estimated solar absorptivity, long-wave radiation, or external convection coefficients. This treatment is appropriate for validating through-thickness conduction against the measured core temperature, but it also means the model cannot independently predict changes due to a different radiation or wind environment unless new surface boundary histories are supplied.

$$T(0, t) = T_{upper}(t) \tag{18}$$

$$T(L, t) = T_{lower}(t) \tag{19}$$

Accordingly, the numerical results should be interpreted as an experimentally forced internal heat-conduction solution rather than a fully coupled outdoor radiation-convection simulation.

Table 4. Initial and boundary conditions for the 1D FVM model.

Location/Quantity	Mathematical Treatment	Source/Role
Initial field, $0 < x < L$	$T(x, 0) = T_0$, uniform	Initialized from first measurement at ~06:00
Upper/exterior surface, $x = 0$	$T(0, t) = T_{upper}(t)$	Measured Dirichlet boundary; includes net environmental heating effects
Lower/interior surface, $x = L$	$T(L, t) = T_{lower}(t)$	Measured Dirichlet boundary
Ambient temperature	$T_{ambient}(t)$ recorded	Supporting environmental variable; not a direct solver boundary
Radiation/external free convection	No separate q_{rad} or h_{conv} term solved	Their combined effect is reflected in measured surface temperatures

2.10. One-Dimensional Conduction Heat Flux

For one-dimensional analysis across the thickness of the brick, the average heat flux is calculated based on Fourier's law:

$$q'' = k\frac{(T_{hot} - T_{cold})}{L} \tag{20}$$

where q'' is the through-thickness conduction heat flux (W/m^2), k is the effective thermal conductivity (W/m·K), Thot is the exterior or upper-surface temperature, T_{cold} is the lower-surface temperature, and L is the brick thickness (m).

The resulting heat flux value has the following thermodynamic interpretation: positive values indicate the influx of heat from the outside to the inside (heating phase), while negative values indicate heat release/solidification from inside the material to the outside environment (cooling phase in the afternoon).

2.11. Numerical Model Validation

The performance of the developed 1D FVM model was evaluated by comparing the simulated temperature profile with the experimental temperature measured at the brick core (T_{core}). The agreement between the simulated and experimental data was assessed using the coefficient of determination (R^2). A value of R^2 close to one indicates that the numerical model can accurately represent the variation in the experimental temperature data:

$$R^2 = 1 - \frac{\sum_{i=1}^{n}\left(T_{exp,i} - T_{sim,i}\right)^2}{\sum_{i=1}^{n}\left(T_{exp,i} - \bar{T}_{exp}\right)^2} \tag{21}$$

where $T_{exp,i}$ and $T_{sim,i}$ are the experimental and simulated temperatures at time i, respectively; $\bar{T}_{exp}$ is the mean experimental temperature; and n is the number of paired observations.

In addition to R^2, the mean absolute error (MAE) and root mean square error (RMSE) were calculated to quantify the average absolute deviation and the quadratic error between the simulated and experimental temperatures. These statistical indicators were used to evaluate both the accuracy and reliability of the numerical model [28,29]:

$$\mathrm{MAE} = \frac{1}{n}\sum_{i=1}^{n}\left|T_{exp,i} - T_{sim,i}\right| \tag{22}$$

$$\mathrm{RMSE} = \sqrt{\frac{1}{n}\sum_{i=1}^{n}\left(T_{exp,i} - T_{sim,i}\right)^2} \tag{23}$$

3. Results and Discussion

3.1. Composite Brick Transient Temperature Profile

The transient temperature profile during the daily testing cycle from 06:00 to 18:00 is shown in Figure 5. The upper surface temperature of the composite brick (T_{upper}) increased rapidly in response to solar radiation and ambient temperature. The maximum upper surface temperature was recorded at 45.52 °C at 12:15. In contrast, the core temperature (T_{core}) increased more gradually and reached its peak value of 44.58 °C at 13:45. This difference in peak time indicates that heat propagation from the exterior surface to the brick core was delayed by approximately 90 min.

The 90-min delay demonstrates substantial thermal inertia of the hybrid wall element during the daytime cycle. The attenuation arises from the combined sensible heat capacity of the brick and hybrid core, the high water-associated heat capacity of the hydrated gel, and the onset of the paraffin phase-change interval. Because the measured core peak of 44.58 °C is only slightly above the lower reported transition temperature of 44 °C, the data do not support a claim of complete paraffin melting. The phase-change contribution should therefore be interpreted as partial activation of latent storage superimposed on dominant sensible/apparent heat-capacity buffering.

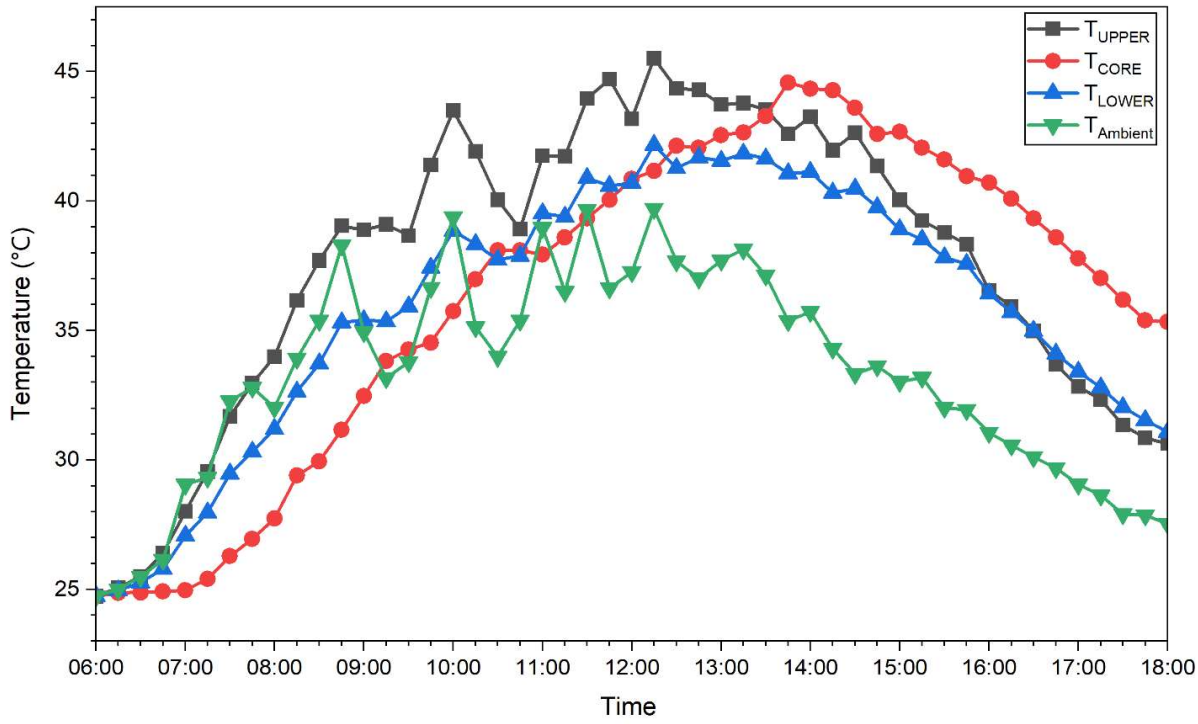


Figure 5. Transient temperature profiles of the hybrid PCM composite brick. The graph illustrates the diurnal variations in the upper surface (T_{upper}), core (T_{core}), lower surface (T_{lower}), and ambient ($T_{ambient}$) temperatures during the outdoor testing cycle (06:00–18:00), highlighting the delayed heat propagation and thermal time lag.

3.2. Characteristics of Conduction Heat Flux

The heat transfer dynamics across the brick thickness were evaluated using the one-dimensional conduction heat flux (q''). As shown in Figure 6, the heat flux was positive during the morning and early afternoon, indicating heat absorption from the exterior surface into the specimen. The maximum heat absorption rate reached 32.50 W/m^2 at 10:00. As solar intensity decreased in the afternoon, the heat flux gradually decreased and became negative at 16:30, with a value of −0.06 W/m^2. The red horizontal line at 0 W/m² represents the zero-flux baseline, which clearly separates the heat absorption phase (positive region above the line) from the heat dissipation phase (negative region below the line). This negative value indicates the beginning of the heat release phase, in which stored thermal energy was dissipated from the material. The maximum heat dissipation rate was −4.76 W/m^2 at 17:30.

The asymmetric transient heat flux pattern was also captured by the developed 1D FVM model. The effective heat capacity formulation enabled the model to represent the transient thermal response associated with latent heat storage in the PCM core. Because the finite volume method conserves energy within each control volume, the model is suitable for describing heat transfer in PCM-based composite materials. The agreement between experimental and simulated trends suggests that the equivalent thermophysical properties used in the model were adequate to represent the overall thermal behavior of the hybrid material system.

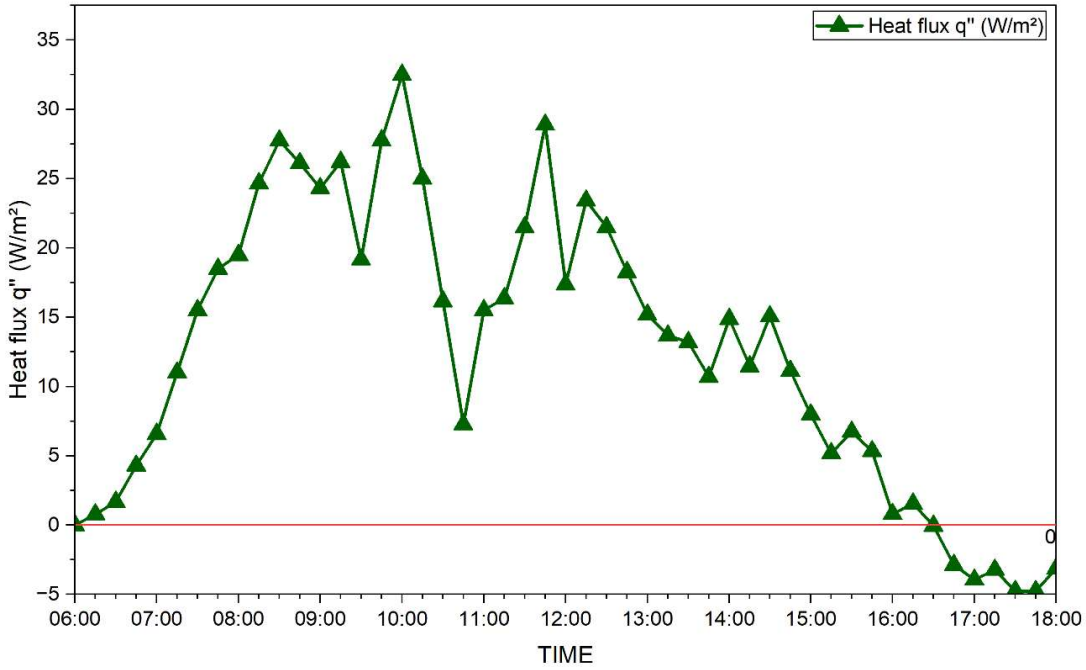


Figure 6. Transient conduction heat flux across the composite brick. The graph depicts the asymmetric dynamic heat absorption (positive values) and heat dissipation (negative values) phases over the 12-h diurnal testing period.

3.3. Thermal Damping Between Brick Layers

The resistance of the composite brick to inward heat penetration was evaluated from transient temperature differences between the measured layers, as presented in Figure 7. These differences quantify thermal damping across the 6.5-cm thickness and are consistent with the one-dimensional analysis direction. They should not be interpreted as an independent proof that all lateral gradients are zero; rather, the 1D assumption is supported by the specimen aspect ratios and by the sensor arrangement used in this study. According to Fourier's law, the through-thickness temperature gradient $\Delta T/\Delta x$ is the driving quantity for conductive heat transfer.

During heating, the maximum absolute temperature difference between the upper surface and the brick core reached 7.88 °C at 08:45, when T_{upper} was 39.05 °C and T_{core} was 31.17 °C. This difference shows that the imposed exterior thermal load was not transferred instantaneously to the core. The behavior is consistent with storage and redistribution of energy within the brick/hybrid system. At the measured temperatures, the contribution of paraffin is better described as the onset of phase-change storage rather than full melting, while zeolite and the hydrated gel primarily provide structural stabilization and sensible thermal buffering.

The overall insulation performance was further evaluated using the temperature difference between the upper and lower surfaces, expressed as ($\Delta T_{upper-lower} = T_{upper} - T_{lower}$). The maximum overall thermal damping reached 4.65 °C at 10:00, when (T_{upper}) was 43.50 °C and (T_{lower}) was 38.85 °C. The maintenance of this temperature difference indicates that the hybrid PCM system acted as a thermal barrier that reduced direct heat transfer across the brick thickness. The combined effects of paraffin, zeolite, and hydrogel ice pack contributed to delayed and attenuated heat propagation, suggesting the potential of this material system to reduce thermal transmission through building envelopes.

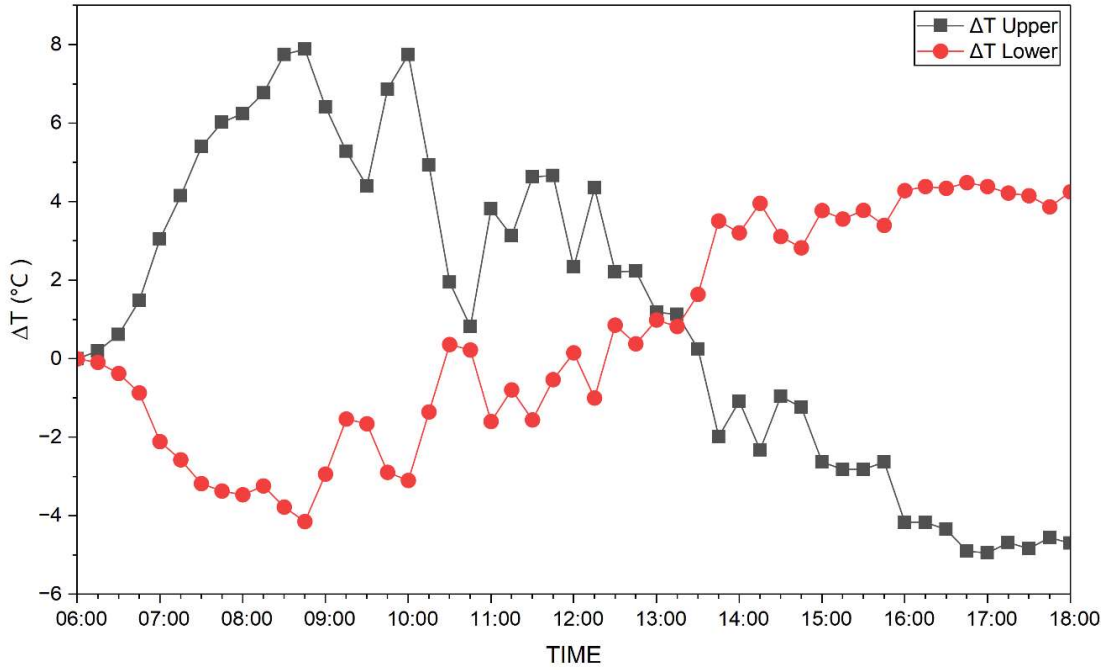


Figure 7. Thermal damping characteristics of the composite brick. The graph presents the transient temperature differences between the upper surface and the core ($\Delta T_{upper\text{-}core}$), demonstrating the thermal attenuation capacity of the hybrid PCM system to resist inward heat penetration.

3.4. Numerical Model Validation

The 1D FVM model was validated by pairing the simulated core temperature with the experimentally measured core temperature at the experimental observation times. Figure 8 presents the parity comparison. The error statistics in Table 5 show MAE = 0.577 °C, RMSE = 0.788 °C, and R^2 = 0.994. Because MAE and RMSE are below 1 °C and the parity points closely follow the 1:1 trend, the model reproduces the measured core-temperature variation with good accuracy over the investigated daytime interval.

Table 5. Statistical validation of simulated versus measured brick-core temperature.

Metric	Value	Interpretation
MAE	0.577 °C	Mean absolute deviation between paired numerical and experimental temperatures
RMSE	0.788 °C	Quadratic error measure; below 1 °C
R^2	0.994	99.4% of experimental temperature variance represented by the model

The coefficient of determination of 0.994 indicates strong agreement for the measured conditions and chosen boundary forcing. The result supports use of the 10-node 1D FVM as a reduced-order tool for the present specimen, but it should not be interpreted as proof of grid independence or as validation of a fully coupled convection-radiation model. The model is validated specifically for internal transient conduction driven by the measured surface temperatures.

The validation also supports the practical use of the effective heat-capacity representation in this reduced temperature range. However, because the core temperature only entered the lower end of the paraffin transition interval, the experiment provides validation mainly for the onset of phase change rather than for a complete melting-solidification cycle. A future 24-h test reaching a larger phase fraction would provide a stronger validation of the latent-heat formulation.

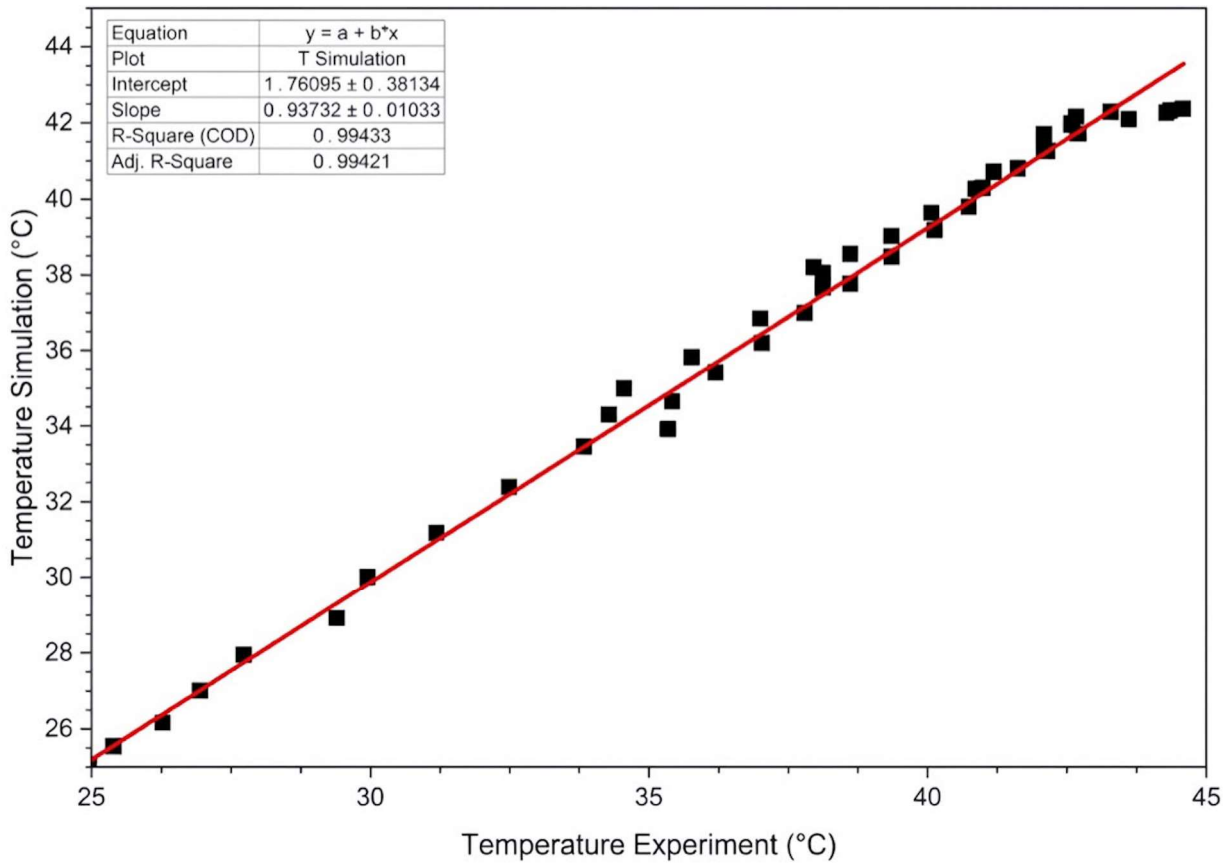


Figure 8. Validation of the 1D FVM numerical model. The scatter plot illustrates the linear correlation and strong statistical agreement ($R^2 = 0.994$) between the simulated and experimentally measured core temperatures.

3.5. Phase-Change Extent, Specific Energy, and Model Scope

Using the linear phase-fraction diagnostic defined in Section 2.5 with $T_s = 44$ °C and $T_l = 60$ °C, the maximum measured core temperature of 44.58 °C corresponds to $f_{l,core} \approx (44.58 - 44)/(60 - 44) = 0.036$, or approximately 3.6% liquid fraction. The maximum measured upper-surface temperature of 45.52 °C gives a theoretical temperature-based upper bound of approximately 9.5% if a local PCM node were to reach that same temperature. Thus, the daytime test activated only the lower portion of the paraffin transition interval; complete melting was not reached.

A mass-normalized energy estimate can be obtained without inventing an unreported cavity mass. Taking the initial core temperature as approximately 25 °C from Figure 5, the sensible contribution of the hybrid core at the 44.58 °C peak is $c_{p,base}\Delta T \approx 2.660 \times (44.58 - 25) = 52.1$ kJ/kg. The paraffin latent contribution per kilogram of hybrid core is $w_p f_l L_p$. With $w_p = 0.40$, $f_l = 0.036$, and $L_p = 160$–210 kJ/kg, this term is approximately 2.3–3.0 kJ/kg. The combined specific absorbed energy is therefore approximately 54.4–55.1 kJ/kg of hybrid core at the measured core peak. This value is an engineering estimate based on literature latent heat and the measured temperature, not a direct calorimetric measurement.

The total absorbed energy in joules would require the actual mass of hybrid PCM placed in the brick cavities. That mass is not reported in the archived manuscript data supplied for this revision, so a total-energy value is intentionally not fabricated. Likewise, conventional two-dimensional temperature or liquid-fraction contour plots are not presented because the implemented model has only one spatial coordinate. A 2D contour would imply lateral resolution that the 1D model does not contain; the physically meaningful numerical field is $T(x, t)$ along the thickness. The 12-h simulation window is consistent with the daytime experimental protocol and captures solar charging plus the onset of afternoon discharge, but it does not characterize the full nocturnal cooling and resolidification process.

4. Conclusions

This study evaluated the daytime thermal-regulation performance of a macro-encapsulated hybrid brick containing 40 wt% paraffin, 30 wt% natural zeolite, and 30 wt% hydrogel ice pack. The measured response showed a 90-min peak-temperature time lag between the upper surface and the brick core, a maximum upper-to-core temperature difference of 7.88 °C, and a maximum upper-to-lower thermal decrement of 4.65 °C. The calculated conduction heat flux reached 32.50 W/m^2 during heat absorption and −4.76 W/m^2 during heat release. The 10-node 1D FVM model reproduced the measured core-temperature trend with MAE = 0.577 °C, RMSE = 0.788 °C, and R^2 = 0.994. A phase-fraction interpretation based on the reported 44–60 °C paraffin transition interval indicates only approximately 3.6% liquid fraction at the measured core peak, showing that the daytime experiment captured the onset rather than completion of paraffin melting. The observed buffering is therefore associated with the combined sensible heat capacity of the composite and partial activation of latent storage. The revised model description also clarifies that radiation and free convection are not solved separately, under-relaxation and mushy-zone constants do not apply to the explicit 1D conduction formulation, and no formal mesh- or time-step-independence claim is made beyond the reported Fourier-number stability assessment. Future work should include measured PCM cavity mass, DSC characterization of the actual hybrid mixture, refined-grid and refined-time-step verification, and a full 24-h experiment to capture complete charging, discharge, and nocturnal resolidification.

Statement of the Use of Generative AI and AI-Assisted Technologies in the Writing Process

During the preparation of this manuscript, AI-assisted technologies (e.g., ChatGPT, GPT-4, OpenAI) were used solely to improve its readability, grammar, and language quality. After using these tools/services, the authors reviewed and edited the content as needed and take full responsibility for the content of the published article.

Acknowledgments

The authors would like to express their sincere gratitude to the Department of Mechanical Engineering and the Research Center of Energy and Nanomaterials at Universitas Muhammadiyah Pontianak for providing research facilities, technical support, and assistance throughout this study. The authors also appreciate the contributions of all research team members involved in material preparation, specimen fabrication, thermocouple installation, experimental data collection, and thermal performance analysis of the hybrid PCM wall system.

Author Contributions

Conceptualization, W.W., I.R., Y.D.A., D.I., M.I., G.G. and R.F.; Methodology, W.W., I.R., Y.D.A., D.I., M.I., G.G. and R.F.; Validation, W.W., I.R., Y.D.A., D.I., M.I., G.G. and R.F.; Formal Analysis, W.W., I.R. and Y.D.A.; Investigation, W.W., I.R. and Y.D.A.; Resources, R.F., D.I., M.I. and G.G; Data Curation, W.W., I.R. and Y.D.A.; Writing—Original Draft Preparation, W.W., I.R. and Y.D.A.; Writing—Review & Editing, W.W., I.R., Y.D.A., D.I., M.I., G.G. and R.F.; Visualization, W.W., I.R. and Y.D.A.; Supervision, D.I., M.I., G.G. and R.F.; Project Administration, D.I., M.I. and G.G.

Ethics Statement

Not applicable.

Informed Consent Statement

Not applicable.

Data Availability Statement

Data will be provided upon request.

Funding

This research received no external funding.

Declaration of Competing Interests

The authors declare that they have no known competing financial interests or personal relationships that could have appeared to influence the work reported in this paper.

References

1. Gupta V, Deb C. Envelope design for low-energy buildings in the tropics: A review. *Renew. Sustain. Energy Rev*. **2023**, 186, 113650. DOI:10.1016/j.rser.2023.113650
2. Masood U, Haggag M, Hassan A, Laghari M. A Review of Phase Change Materials as a Heat Storage Medium for Cooling Applications in the Built Environment. *Buildings* **2023**, *13*, 1595. DOI:10.3390/buildings13071595
3. Nabwey HA, Tony MA. Enhancing the performance of paraffin's phase change material through a hybrid scheme utilizing sand core matrix. *Sci. Rep.* **2024**, *14*, 20755. DOI:10.1038/s41598-024-71848-8
4. Al-Yasiri Q, Szabó M. Incorporation of phase change materials into building envelope for thermal comfort and energy saving: A comprehensive analysis. *J. Build. Eng.* **2021**, *36*, 102122. DOI:10.1016/j.jobe.2020.102122
5. Qin P, Wang H, Gong N, Cai X, Wang H, Hou F. Experimental and Numerical Investigation of Heat Transfer Characteristics of Double-Layer Phase Change Walls for Enhanced Thermal Regulation in Summer Climates. *Buildings* **2025**, *15*, 962. DOI:10.3390/buildings15060962
6. Fahrezi D, Irawan D, Iwan M, Julianto E, Fahrurrozi F, Govari MK. Experimental Study of Conduction Heat Transfer Using Paraffin Phase Change Material on Bricks. *Int. J. Ind. Innov. Mech. Eng.* **2024**, *2*, 60–72. DOI:10.61132/ijiime.v2i1.120
7. Huang Y, Alekhin VN, Hu W, Pu J. Adaptability Analysis of Hollow Bricks with Phase-Change Materials Considering Thermal Performance and Cold Climate. *Buildings* **2025**, *15*, 590. DOI:10.3390/buildings15040590
8. Ghafoorian F, Mehrpooya M, Shafiee M. A comparative study of the performance of lattice structures embedded with phase change materials as thermal conductivity enhancers. *Int. J. Heat Fluid Flow* **2026**, *117*, 110000. DOI:10.1016/j.ijheatfluidflow.2025.110000
9. Huang Y, Yuan R, Miao C. Influence of phase change materials on the thermal performance of hollow bricks under cold climate conditions: An experimental study. *E3S Web Conf.* **2024**, *542*, 01009. DOI:10.1051/e3sconf/202454201009
10. Rai AC. Energy performance of phase change materials integrated into brick masonry walls for cooling load management in residential buildings. *Build. Environ.* **2021**, *199*, 107930. DOI:10.1016/j.buildenv.2021.107930
11. Bhamare DK, Rathod MK, Banerjee J, Arıcı M. Investigation of the Effect of Air Layer Thickness on the Thermal Performance of the PCM Integrated Roof. *Buildings* **2023**, *13*, 488. DOI:10.3390/buildings13020488
12. Voigt I, Schmerler R, Korn H, Drossel WG. Heat-Transfer Properties of Additively Manufactured Aluminum Lattice Structures in Combination with Phase Change Material. *Materials* **2024**, *17*, 1672. DOI:10.3390/ma17071672
13. Mehrpooya M, Mirmotahari SR, Ghafoorian F, Karimkhani M, Ganjali MR. Investigation of a packed bed energy storage system with different PCM configurations and heat transfer enhancement with fins using CFD modeling. *Chem. Pap.* **2024**, *78*, 2453–2467. DOI:10.1007/s11696-023-03251-y
14. Lee SJ, Park SH. Effects of Superabsorbent Polymer Addition on the Thermal Properties of Eutectic Phase Change Material. *Processes* **2024**, *12*, 162. DOI:10.3390/pr12010162
15. Choi J, Valtchev V, Moteki T, Ogura M. Phase Change Material-Containing Mesoporous Zeolite Composite for Adsorption Heat Recovery. *Adv. Mater. Inter.* **2021**, *8*, hal-03035395. DOI:10.1002/admi.202001085
16. Qiu L, Murashov V, White MA. Zeolite 4A: Heat capacity and thermodynamic properties. *Solid State Sci.* **2000**, *2*, 841–846. DOI:10.1016/S1293-2558(00)01102-X
17. Chang Z, Sun S, Ji Y, Wang G. Estimation of Thermal Properties of Solid–Liquid Phase Change Material Using Fuzzy Inference Methods. *J. Thermophys. Heat Transf.* **2024**, *38*, 630–637. DOI:10.2514/1.T6978
18. Alvarez-Rodriguez M, Alonso-Martinez M, Suarez-Ramon I, José García-Nieto P. Numerical model for determining the effective heat capacity of macroencapsulated PCM for building applications. *Appl. Therm. Eng.* **2024**, *242*, 122478. DOI:10.1016/j.applthermaleng.2024.122478

19. Versteeg HK, Malalasekera W. An Introduction to Computational Fluid Dynamics Second Edition. 2007. Available online: www.pearsoned.co.uk/versteeg (accessed on 5 August 2026).
20. Didi F, Kareem AK, Rodrigues P, Widatalla S, Khan SA, Abbas H, et al. Investigation of the solidification process of phase change materials and the heat transfer interactions between PCM and fins in a two-dimensional cylindrical latent heat energy storage system. *Int. Commun. Heat Mass Transf.* **2025**, *169*, 109838. DOI:10.1016/j.icheatmasstransfer.2025.109838
21. Kahwaji S, Johnson MB, Kheirabadi AC, Groulx D, White MA. A comprehensive study of properties of paraffin phase change materials for solar thermal energy storage and thermal management applications. *Energy* **2018**, *162*, 1169–1182. DOI:10.1016/j.energy.2018.08.068
22. Rubitherm Technologies GmbH, RT50 Data Sheet. Version 09.10.2020. Available online: https://www.rubitherm.eu/media/products/datasheets/Techdata_-RT50_EN_09102020.PDF (accessed on 5 August 2026).
23. Jadhav R, Sable MJ, Bhalla V, Jadhav PK, Sawant HH, Konkala B, et al. Optimization of Fin Arrangements in Latent Heat Storage Systems. *Math. Model. Eng. Probl.* **2025**, *12*, 601–608. DOI:10.18280/mmep.120223
24. Fauzi M, Kurniawan B, Fachredzy A, Nabawi MAH, Tetuko AP. Paraffin-Based Phase Change Materials (PCM) with Enhanced Thermal Conductivity Through Particle Addition and Encapsulation Techniques for Thermal Energy Storage: A Critical Review of Materials Science. *Trends Sci.* **2025**, *22*, 10308. DOI:10.48048/tis.2025.10308
25. Shen Y, Liu S, Zeng C, Zhang Y, Li Y, Han X, et al. Experimental thermal study of a new PCM-concrete thermal storage block (PCM-CTSB). *Constr. Build. Mater.* **2021**, *293*, 123540. DOI:10.1016/j.conbuildmat.2021.123540
26. Malkawi DS, Rabady RI, Malkawi MS, Al Rabadi SJ. Application of Paraffin-Based Phase Change Materials for the Amelioration of Thermal Energy Storage in Hydronic Systems. *Energies* **2022**, *16*, 126. DOI:10.3390/en16010126
27. Li H, Ke X, Zheng W, Si Y, Cao W, Lv W, et al. Research on an Improved Adaptive Optimization Calculation Method for Dynamic Heat Flux of Building Envelope Based on IFDM-RKF. *Energies* **2026**, *19*, 1641. DOI:10.3390/en19071641
28. Zhu L, Wang Q, Sang G, Cao Z, Xue Y. Experimental and Numerical Study on the Thermal Response of the Lightweight Aggregate Concrete Panels Integrated with MPCM. *Buildings* **2024**, *14*, 234. DOI:10.3390/buildings14010234
29. Karimi S, Mehrpooya M, Pourfayaz F, Ghafoorian F. A Comprehensive Parametric CFD Investigation on Packed Bed Thermal Energy Storage System with Encapsulated Solid–Solid Phase Change Materials in Discharging Mode. *Arab. J. Sci. Eng.* **2025**, *50*, 2351–2365. DOI:10.1007/s13369-024-09077-4